ORIGINAL ARTICLE

Journal
American Ceramic Society

Preparing Li-garnet electrodes with engineered structures by phase inversion and high shear compaction processes

Fengyu Shen[1] | Robert A. Jonson[1] | Dilworth Y. Parkinson[2] | Michael C. Tucker[1]

[1]Energy Storage and Distributed Resources Division, Lawrence Berkeley National Laboratory, Berkeley, CA, USA

[2]Advanced Light Source, Lawrence Berkeley National Laboratory, Berkeley, CA, USA

Correspondence
Fengyu Shen and Michael C. Tucker, Energy Storage and Distributed Resources Division, Lawrence Berkeley National Laboratory, Berkeley, CA, USA.
Email: fshen@lbl.gov (F. S.); mctucker@lbl.gov (M. C. T.)

Abstract

Solid-state lithium batteries are promising for safety and energy density compared with traditional lithium-ion batteries. However, the large interfacial resistance between the electrode and electrolyte is a bottleneck to achieving high-performance solid-state batteries. Engineered electrode structures with a porous scaffold of the solid electrolyte material are promising to lower the interfacial resistance and provide a mechanical support for a thin solid electrolyte layer. In this work, two ceramic processing techniques are used to fabricate porous/dense bilayer architectures based on a $Li_{6.25}Al_{0.25}La_3Zr_2O_{12}$ (LLZO) Li-garnet material. Finger-like vertically aligned pores are created by the phase inversion (PI) process. A water bath presaturated with Li salt prevents Li loss during the PI solvent exchange step. Pore size and porosity can be optimized by adjusting the bath temperature. The high shear compaction process was used to prepare LLZO tapes with 40, 60, and 80 vol% poreformer. The porosity of the tapes after sintering is 39.5%, 58.4%, and 75.4%, respectively. Microtomography exhibits the porosity, pore shape, and pore distribution of the tapes. A typical cathode material $LiNi_{0.33}Mn_{0.33}Co_{0.33}O_2$ (NMC) is filled into the pores *via* vacuum infiltration, and a dense cathode layer is formed within the garnet scaffold.

KEYWORDS
garnet, infiltration, LLZO, porous scaffold, solid-state battery

1 | INTRODUCTION

Lithium-ion batteries are widely used in portable devices and electric vehicles.[1] The inherent safety issues of conventional lithium-ion batteries, such as explosion, fire, and leakage of organic electrolyte, are significant.[2,3] Solid-state batteries (SSBs), as the next generation of battery technology, have gained extensive attention in recent years because of their high safety and potential compatibility with lithium metal anode.[4,5] Garnet electrolytes show ionic conductivity greater than 1 mS cm^{-1} at room temperature,[6,7] which is sufficiently high to support reasonable current densities in lithium metal battery configurations. Ceramic electrolytes exhibit poor interfacial contact with electrodes, however, and they are generally thick and brittle leading to high ohmic impedance and mechanical failure.[8,9] The specific energy density is still low because of the high density of ceramics.[10] In addition, it is challenging to fabricate garnet electrolytes, such as Al-doped $Li_7La_3Zr_2O_{12}$ (LLZO), with thickness <100 μm without any support,[11] which means the lithium-ion conduction pathway between the electrodes is long. The porous scaffold/dense electrolyte structure makes it feasible to have a thin (tens of microns) electrolyte, leading to lower ohmic impedance, as the thick porous scaffold can provide mechanical support.

Using a porous ceramic scaffold to support a thin ceramic electrolyte is a mature technique and has been

widely applied in solid oxide fuel cells,[12,13] filters,[14,15] and SSBs.[16–18] To fabricate porous scaffold for SSBs, tape casting,[19,20] freeze tape casting,[21–24] templating,[25,26] electrospinning,[27–29] 3D printing,[30,31] etc., have been demonstrated. Most of these methods create porous structures with high tortuosity, leading to long lithium-ion diffusion pathways and challenges for infiltrating solid active material particles, and these methods may not scale well because of low throughput, complicated processing, or high cost.

The phase inversion (PI) process has been widely used in numerous chemical industries, biotechnology, environmental separation, and energy conversion and can fabricate large-area porous scaffolds with low cost.[32–34] It has also been used to construct microchannels of $Li_{0.34}La_{0.51}TiO_3$ for SSBs.[35] The PI process creates finger-like pores when the solvent in a slurry of ceramic particles, binder, and dispersant counter-diffuses with a nonsolvent liquid placed in contact with the slurry surface. During the PI procedure, water is typically used as the nonsolvent to induce phase separation. Water reacts with most battery materials, however, which is one reason why the PI process has not been widely applied in the battery community. The high shear compaction (HSC) process is a ceramic tape fabrication technique developed by Ragan Technologies. It densifies powders and binders by compaction to form large-area thin tapes. HSC is capable of preparing tapes with high quality and excellent dimensional tolerance, without separation of the ceramic, poreformer, and binder phases. This process is commonly used in manufacturing production of ceramic substrates due to its low cost, high production throughput and good control of shrinkage.[36,37]

In this work, LLZO scaffold electrodes with engineered structures were fabricated by PI and HSC processes, and incorporated into bi-layer architectures. HSC has not been reported previously to fabricate battery components. Large area porous tapes with vertically aligned finger-like pores were fabricated by the PI process, and the intended cubic phase was obtained after sintering when using a water bath that was saturated with Li_2CO_3. The porosity of HSC tapes was adjusted and the highest porosity of 75.4% was achieved. Pores in both tapes were successfully filled with $LiNi_{0.33}Mn_{0.33}Co_{0.33}O_2$ (NMC) cathode material, with good contact between the cathode and the scaffold.

2 | EXPERIMENTAL

2.1 | Preparing dense tapes by tape casting

Commercial Al-doped LLZO powder (Ampcera, USA) was used in this study. Dense tapes were prepared by tape casting with solvent-based binder (Polymer Innovation Inc.).[38] Briefly, LLZO powder (5 g), Li_2CO_3 (0.3 g), and MgO (0.1 g) were mixed in a Teflon bottle with 30 g of ZrO_2 balls. MgO acts as a sintering aid and limits the LLZO grain growth. Toluene solvent (4.5 g) and DS002 dispersant (0.1 g, Polymer Innovations, Inc.) were added subsequently. The mixture was ball-milled overnight. MSB1-13 binder (2 g, Polymer Innovations, Inc.) was then added, and the suspension was ball-milled for another 4 h. After tape casting onto Si-coated Mylar substrates, the tapes were dried naturally and peeled off the substrate.

2.2 | Preparing porous tapes by phase inversion

LLZO powder (5 g), Li_2CO_3 (0.3 g) and MgO (0.1 g) were mixed in a Teflon bottle with 30 g ZrO_2 balls. N-Methyl-2-pyrrolidone solvent (NMP, 4.5 g) and polyvinylpyrrolidone dispersant (0.05 g) were added. After ball milling for 4 h, polyethersulfone (PESF, 0.322 g) was added into the suspension, followed by 2 h of ball milling. PL008 (0.1 g, Polymer Innovation Inc.) was added to improve wetting on the Mylar casting substrate, followed by 30 min of ball milling.

The prepared LLZO suspension was tape cast on Si-coated Mylar substrate and soaked immediately in a water bath with deionized (DI) water or Li_2CO_3-saturated water. After solvent exchange completed, the tape was removed from the water bath and dried overnight in ambient air. The PI process is illustrated in Figure 1A. Bi-layer structures were prepared by casting the LLZO slurry onto a dry, pre-formed electrolyte tape, followed by PI. Lamination or hot pressing are not needed to achieve good bonding between the porous and dense layers.

2.3 | Preparing porous tapes by high shear compaction

High shear compaction tapes were prepared by Ragan Technologies, whose full-scale continuous process is illustrated in Figure 1B. Samples were prepared with lab-scale procedures that mimic the full-scale process. LLZO slurry was prepared with LLZO (5 g), Li_2CO_3 (0.3 g), MgO (0.1 g), 12.3 wt% commercial binder, and polymethyl methacrylate (PMMA, Sunjin Chemical Co. Ltd) poreformer (40, 60, 80 vol%). Water was used as the solvent. The size of PMMA is ~60 μm, and the thickness of the tape is about 200 μm. HSC tapes were laminated with dense tapes at 100°C and 100 MPa for 15 min to make bilayer structures.
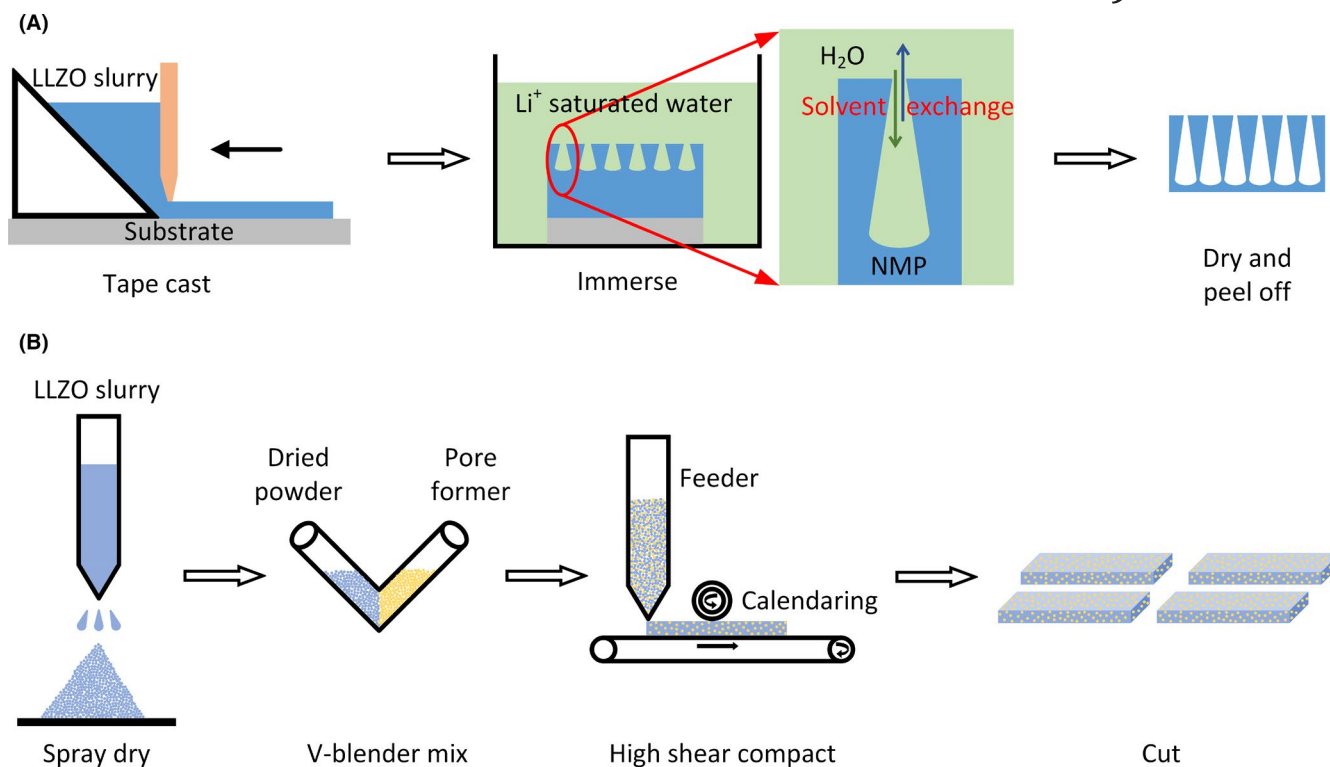
FIGURE 1 Schematic of porous structure formation. (A) phase inversion and (B) high shear compaction processes

2.4 | Sintering

Tapes were cut into the desired shape and size and debinded at 700°C for 1 h in air with heating rate of 1°C min^{-1}. They were sandwiched between two thin Al_2O_3 sheets to prevent warping during debinding. The debinded tapes were sintered at 1125°C for 5 h in Ar atmosphere with heating and cooling rate of 5°C min^{-1}. During sintering, graphite sheets were inserted between the tapes and Al_2O_3 sheets to prevent reaction.

2.5 | Cathode infiltration

NMC (MTI Corporation) was dispersed in NMP (Sigma Aldrich) solvent and ball-milled for 48 h to obtain submicron-scale particles. The NMC suspension was drop cast on bilayer structures and infiltrated under vacuum with pressure of 200 mbar. The tapes were dried under vacuum at 60°C for 5 h to evaporate the NMP solvent.

2.6 | Characterization

The cross section and surface of tapes were observed using a tabletop scanning electron microscope (SEM, JSM-7500F, JOEL). Tapes were mounted in epoxy, cut, and dry polished with aluminum oxide sandpapers (320, 600, 1000, and 1400 grit) to obtain a flat cross section. The crystal structure of sintered tapes was characterized by X-ray diffraction (XRD, D2 Phaser, Bruker), with 10° min^{-1} scanning speed at 0.02° step size. The concentration of chemical elements in the samples was measured by inductively coupled plasma optical emission spectrometry (ICP-OES, Optima 5300 DV, Perkin Elmer). Microtomography was conducted at the Advanced Light Source (ALS) Beamline 8.3.2 at Lawrence Berkeley National Laboratory, with a pixel size of 0.65 µm. Images were collected over 180 degrees in 0.072-degree steps, with 24 keV X-ray. The dark field images were collected to deduct detector dark counts with the X-ray shutter closed, and the bright field images were collected before and after the sample scan to normalize for variations in the incident illumination. The 3D reconstructions were performed with TomoPy, and the images were visualized and analyzed with Avizo software. Energy-dispersive X-ray spectroscopy (EDS) analysis used the secondary electron detector of a field-emission scanning electron microscope (Zeiss Gemini Ultra-55) with a beam energy of 20 kV.

3 | RESULTS AND DISCUSSION

3.1 | Phase inversion

During the PI process, solvent exchange was initially carried out at ~0°C for 30 min, with DI water as the nonsolvent. Rapid exchange of water and NMP occurs between

the interface, causing the precipitation of PESF along with the LLZO powder because of its limited solubility in water. During this process, Li$^+$/H$^+$-exchange caused severe delithiation of the LLZO slurry in the water bath.[39,40] After sintering at 1125°C for 5 h, only the Li-deficient La$_2$Zr$_2$O$_7$ phase is detected by XRD (Figure S1). Severe Li loss was observed even if extra Li$^+$ source (Li$_2$CO$_3$) was added into the LLZO slurry. To overcome this issue, the DI water was replaced with Li$_2$CO$_3$ saturated water, and this effectively prevented the Li$^+$/H$^+$-exchange. In addition, the Li salt in the residual water is retained in the LLZO tape after drying and can compensate for subsequent Li loss during sintering. The ICP-OES data are shown in Table S1, as well as their calibration fitting in Figure S2. The normalized stoichiometry of Li:Al:La:Zr by La-content is 7.08:0.24:3:2.17. As a reference, the stoichiometry of the LLZO green powder is 6.52:0.21:3:2.20. The sintered tape is Li-rich because extra Li sources are added to the PI slurry and water bath, to compensate for Li loss during sintering and prevent Li exchange during PI, respectively. During sintering, MgO acts as a sintering aid and is not doped into the LLZO unit cell.[38] The XRD pattern of the sintered tape shows cubic LLZO phase with two tiny peaks at 25.9 degrees and 27.8 degrees, which is unsure what belongs to (Figure S1). The lattice parameter is calculated to be 12.991 Å, which

is a little higher than the 12.96–12.97 Å reported for dense tapes.[38] The expand lattice parameter can be ascribed to the extra Li in the PI tape.

Phase inversion introduces vertical and finger-like pores (Figure 2A). The depth of the pores is ~120 μm, and the pores do not completely penetrate to the bottom of the tape. There is a dense layer with a thickness of 20 to 30 μm at the bottom. A magnified image for a typical pore is shown in Figure 2B. Microtomography was used to characterize the pore shape and distribution. Vertical pore shape was confirmed throughout the imaging volume (Figure 2C). The average porosity of the sintered tape prepared at 0°C is ~37%, and the porosity changes along the thickness (Z coordinate). It is ~30% at the top surface and increases in the bulk, then suddenly decreases to zero at the dense bottom layer. The average pore area has a similar distribution. An illustration of the average pore shape derived from the pore area curve is shown in the inset of Figure 2D. The pore is largest in the middle, necks gradually at the top, and pinches off suddenly at the bottom.

The porosity and pore size can be adjusted by changing the water bath temperature. Higher bath temperature increases the solvent exchange kinetics and limits the growth of pores. As the temperature rises from 0 to 50°C, the porosity and pore size decrease gradually, as seen in
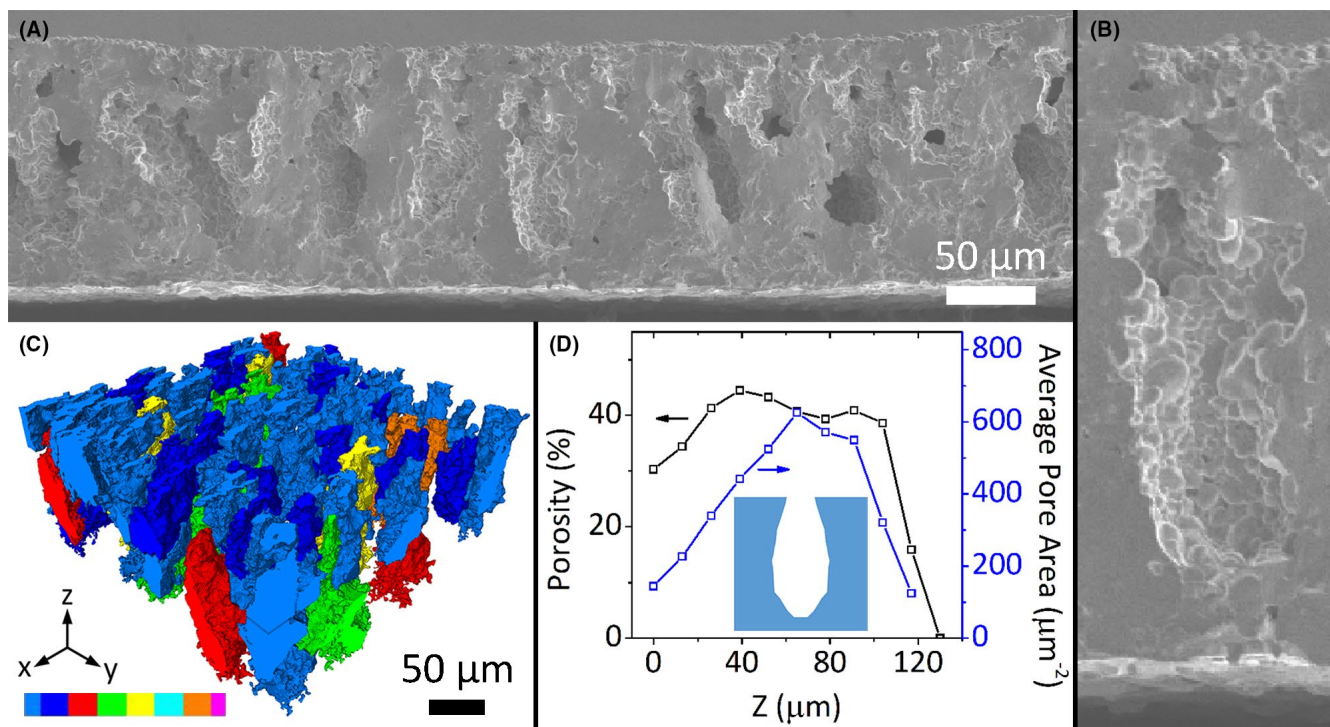

FIGURE 2 Phase inversion (PI) microstructure. SEM images of (A) a fracture section of the sintered tape prepared by PI with Li$^+$ saturated water and (B) high magnification; (C) 3D microtomography pore distribution (D) and corresponding porosity and average pore area distribution along the _z_ direction. Color map is used to distinguish pore size range, from large (light blue) to small (pink). The schematic pore shape based on the average pore size distribution along _z_ direction is shown as an inset in (D)

the tomography xyz slices and average porosity data in Figure 3. The porosity ranges from 10% to 37% when PI is carried out at 50 and 0°C, respectively.

Bilayer structures were fabricated by casting the PI layer on top of a pre-formed tape cast electrolyte layer. The bilayer structure was co-sintered successfully, with excellent adhesion between the layers and full densification of the electrolyte layer (Figure S3). The pores at the top surface are small, 3 to 7 μm (Figure S3b), and the grain size on the electrolyte surface is roughly 5 to 10 μm. Although it is interesting to demonstrate the fabrication of a bilayer structure with this approach, the additional electrolyte layer appears unnecessary, as the bottom layer of the PI structure is already dense.

3.2 | High shear compaction

The HSC tape with 40 vol% PMMA was sintered at 1125°C for 5 h, and pure cubic phase was obtained except for two tiny peaks at 25.9 degrees and 27.8 degrees, similar to the PI tape (Figure S1). The ICP-OES data in Table S1 show that the stoichiometry of Li:Al:La:Zr is 6.97:0.26:3:2.23. The lower Li content in the HSC tape than the PI tape could be due to extra Li_2CO_3 not being used to saturate the water solvent during the HSC tape preparation. The lattice parameter is calculated to be 12.962 Å, which is similar to the dense tapes.[38] The sintered tape is ~150 μm thick and contains round pores diameter ranging from 30 to 60 μm (Figure 4A). In contrast to the pore shape in the PI tape, the HSC pores are nearly spherical and only slightly elongated in the x-y plane, presumably due to deformation during compaction or anisotropic shrinkage during sintering

(Figure 4B). The average porosity of the sintered tape is 39.5%, close to the volume loading of PMMA (40 vol%) in the green tape. The porosity distributes uniformly along the Z direction and the average pore area also distributes uniformly (Figure 4C).

The porosity of the sintered HSC tapes can be adjusted by changing the PMMA loading in the green tapes (Figure 5). Microtomography analysis indicates the porosity of the three tapes prepared with 40, 60, and 80 vol% PMMA is 39.5%, 58.4%, and 75.4%, respectively. The microstructure of bilayers assembled by laminating tape-cast electrolytes to the HSC layers is shown in Figure S4. The bilayer structure provides excellent adhesion between the layers and good densification of the scaffold and the approximately 25-μm-thick electrolyte layer. In contrast to the PI structure, there are large open pores on the HSC top surface (Figure S4d), which is beneficial for cathode filling. The grain size is around 5 to 10 μm, similar to the PI tape.

3.3 | Ionic conductivity and NMC filling

The ionic conductivity of the LLZO scaffolds was measured using the sample geometries shown in Figure 6A. As the sintered PI structure (solvent exchanged at 0°C) is dense on the bottom and has very small pore size (3–7 μm) on the top, silver paste was directly cast on both sides as the electrical contact for electrochemical impedance spectroscopy (EIS) analysis. HSC tapes have larger pores (30 to 60 μm) on both sides, and silver paste could fill the pores when the paste is wet. Therefore, a thin (~20 μm) and dense LLZO layer was laminated on both sides of the porous tapes to have dense/porous/dense
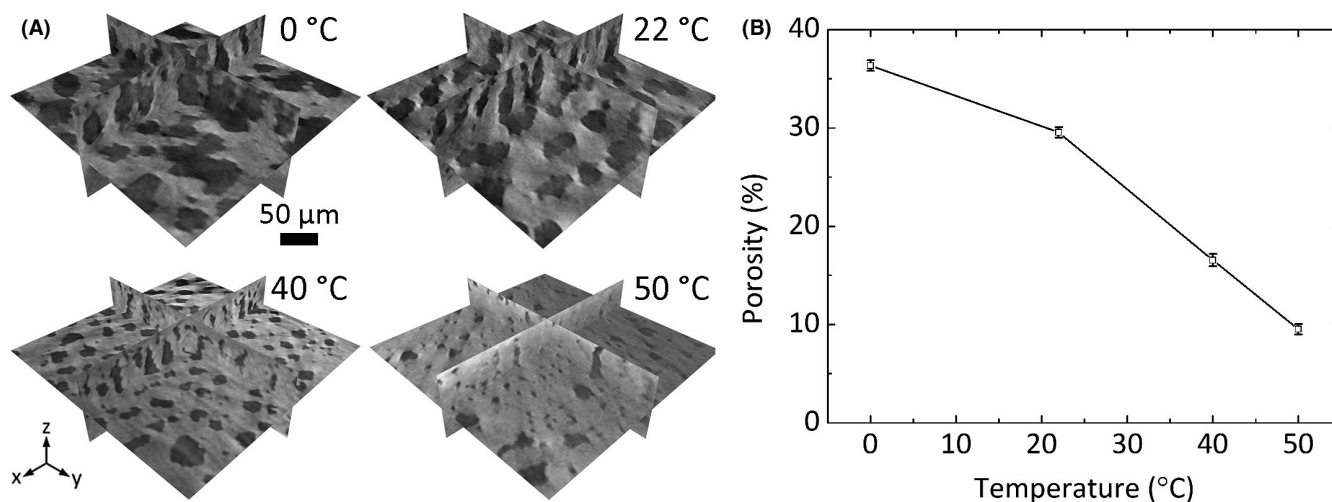

FIGURE 3 Microtomography analysis of sintered phase inversion (PI) tapes prepared at various inversion temperatures. (A) Image slices of PI tapes prepared at 0, 22, 40, and 50°C. The darker areas are pores. (B) The relationship of average porosity with water bath temperature
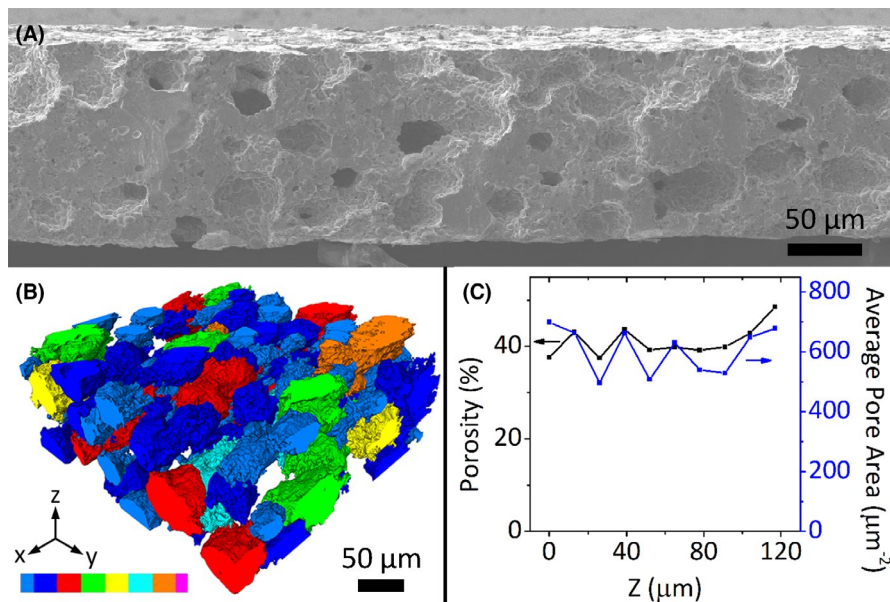
FIGURE 4 High-shear-compaction microstructure. (A) SEM image of a fracture section of the sintered tape prepared with 40 vol% polymethyl methacrylate; (B) Microtomography 3D pore distribution (C) and corresponding porosity and average pore area distribution along z direction. Color map is used to distinguish pore size range, from large (light blue) to small (pink)
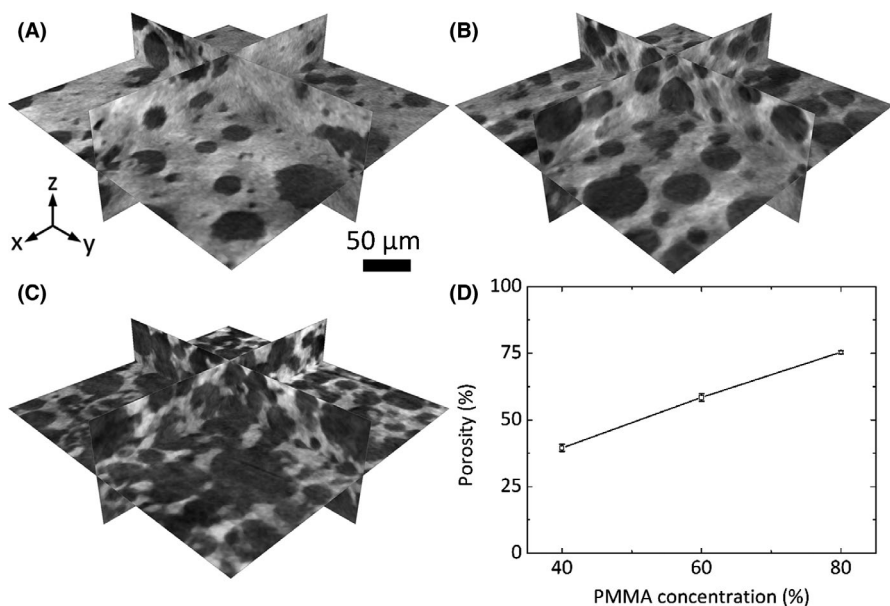

FIGURE 5 Microtomography analysis of sintered high-shear-compaction (HSC) tapes with various poreformer loadings. Image slices of HSC tapes prepared with (A) 40 vol%, (B) 60 vol%, and (C) 80 vol% polymethyl methacrylate (PMMA). (D) The relationship of the sintered porosity with PMMA loading in the green tape. The darker areas are pores

trilayer structure after sintering. An image of the trilayer structure prepared from HSC tape with 60 vol% PMMA is shown in Figure S5. Typical EIS[41–43] for LLZO material is shown in Figure 6B, where the first semicircle is ascribed to the bulk conductivity, and the second semicircle is ascribed to the grain boundary conductivity. The effective ionic conductivity based on total geometric area of the PI tape with 37% porosity is 6.4×10^{-5} S cm^{-1}, and 1.0×10^{-4}, 6.2×10^{-5}, and 1.2×10^{-5} S cm^{-1} for the HSC tapes with 40, 60, and 80 vol% PMMA, respectively. These values are not normalized by the porosity. For comparison, thin dense electrolyte layers prepared with the same powder provide ~2×10^{-4} S cm^{-1}. As expected, the porosity decreases the effective conductivity.

High interfacial resistance between the solid electrolyte and the cathode lowers the performance of SSBs. Infiltrating cathode material into an LLZO scaffold is a useful approach to lower the electrolyte/cathode resistance. Here, a proof-of-concept was carried out by infiltrating NMC into the PI and HSC porous scaffolds. The NMC was ball-milled to reduce the particle size sufficiently to penetrate into the pores. NMC is clearly observed inside the bilayer structures with PI and HSC porous layers (Figure 7). EDS mapping shows the elemental distribution of Zr and Co for the HSC tape, demonstrating the successful infiltration of the NMC into the scaffold. A layer of NMC with the thickness of several hundred nanometers covers the LLZO scaffold with good contact. Even locations at the buried interface of the scaffold and electrolyte were covered
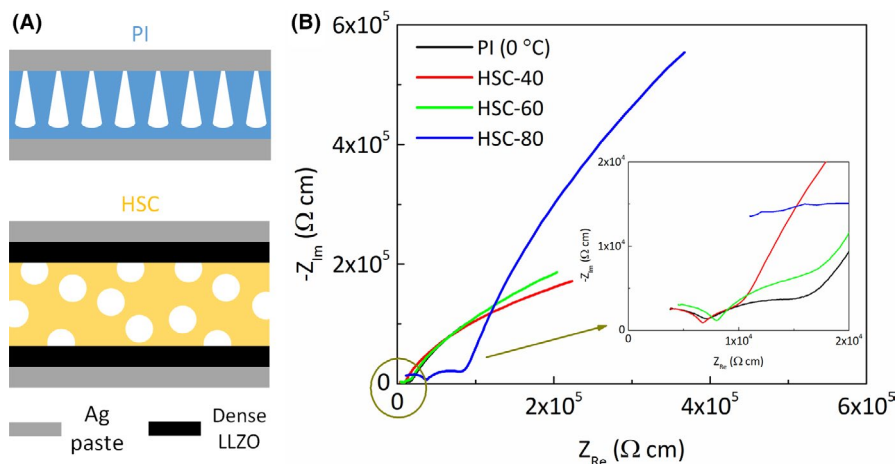
FIGURE 6 Measurement of ionic conductivity. (A) Schematic of the ionic conductivity sample geometry for the phase inversion (PI) and high-shear-compaction (HSC) tapes; (B) Impedance spectroscopy of the sintered PI porous tape (0°C) and HSC-40, 60, and 80 dense/porous/dense trilayer tapes at room temperature, converted to Ohm cm

FIGURE 7 NMC filled into sintered porous/dense bilayer structures. (A and B) phase inversion (PI) (0°C) and (C and D) high shear compaction (80 vol% polymethyl methacrylate [PMMA]) tapes, (E) X-ray diffraction patterns of the PI and HSC tapes with NMC filling. Energy-dispersive X-ray spectroscopy mapping of Zr and Co corresponds to the image (D) at the same magnification
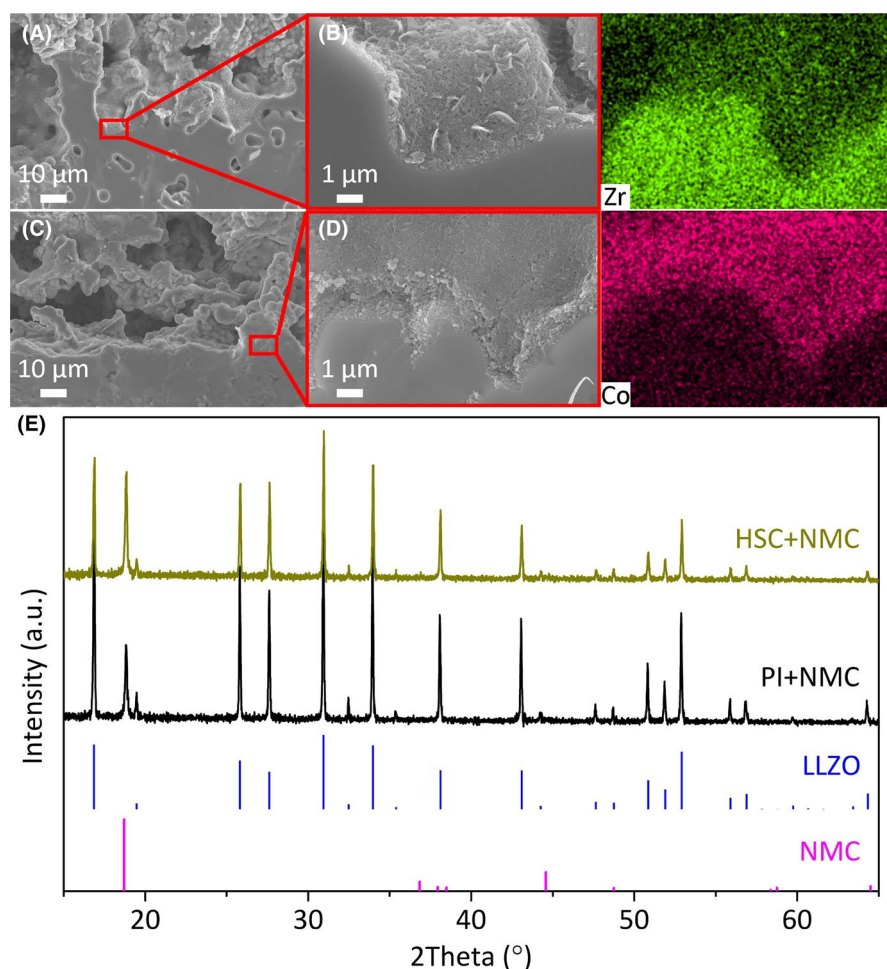
by NMC, confirming the connectivity of the pores. Multiple cycles of infiltration are needed to load more NMC cathode, as the pores are not filled completely after the one-cycle infiltration demonstrated here. XRD patterns (Figure 7E) of the PI and HSC tapes with NMC infiltration match the cubic LLZO and NMC phases, indicating no reaction between LLZO and NMC after drying at 60°C. In addition, no reaction between LLZO and the solvent NMP was detected. Bilayer structures prepared with 40 and 60 vol% PMMA were also successfully infiltrated with NMC (Figure S6).

4 | CONCLUSIONS

Finger-like vertically aligned pore tapes and highly porous tapes were prepared by PI and HSC processes, respectively.

Bilayer structures with dense electrolyte and porous scaffold layers were also prepared. A Li_2CO_3-saturated water bath is effective to inhibit Li loss during PI solvent exchange. The porosity of the PI tapes can be increased to ~37% by lowering the water bath temperature to 0°C. The PI pore size is larger at the middle and smaller at the top and bottom. The PI porous/dense bilayer structure was prepared without lamination or hot press; thus, the vertical pores can be preserved without damage. In addition, the unique architecture of PI tapes makes it possible to prepare an integrated electrolyte without merging a separate dense layer, as the finger-like pores do not penetrate the whole layer. Future optimization will focus on increasing the total porosity and penetration of the pores through the top surface. HSC tapes were prepared with 40, 60, and 80 vol% PMMA and the highest porosity achieved after sintering was 75.4%. The porous/dense bilayer structure, prepared through lamination, provides a thin densified electrolyte supported on a highly porous scaffold. A typical cathode material, NMC, was successfully infiltrated into PI and HSC pores, with good contact between NMC and LLZO. This demonstrates the possibility of cathode filling for full cell assembly in the future.

ORCID
Fengyu Shen https://orcid.org/0000-0003-3818-176X

REFERENCES
1. Goodenough JB, Park KS. The Li-ion rechargeable battery: a perspective. J Am Chem Soc. 2013;135(4):1167–76.
2. Albertus P, Babinec S, Litzelman S, Newman A. Status and challenges in enabling the lithium metal electrode for high-energy and low-cost rechargeable batteries. Nat Energy. 2018;3(1):16–21.
3. Xia SX, Wu XS, Zhang ZC, Cui Y, Liu W. Practical challenges and future perspectives of all-solid-state lithium-metal batteries. Chem-Us. 2019;5(4):753–85.
4. Ould Ely T, Kamzabek D, Chakraborty D. Batteries safety: recent progress and current challenges. Front Energy Res. 2019. 7.
5. Cheng XB, Zhang R, Zhao CZ, Zhang Q. Toward safe lithium metal anode in rechargeable batteries: a review. Chem Rev. 2017;117(15):10403–73.
6. Kim A, Woo S, Kang M, Park H, Kang B. Research progresses of garnet-type solid electrolytes for developing all-solid-state Li batteries. Front Chem. 2020;8.
7. Rettenwander D, Redhammer G, Preishuber-Pflugl F, Cheng L, Miara L, Wagner R, et al. Structural and electrochemical consequences of Al and Ga cosubstitution in $Li_7La_3Zr_2O_{12}$ solid electrolytes. Chem Mater. 2016;28(7):2384–92.
8. Shen FY, Dixit MB, Zaman W, Hortance N, Rogers B, Hatzell KB. Composite electrode ink formulation for all solid-state batteries. J Electrochem Soc. 2019;166(14):A3182–A88.
9. Shen FY, Dixit MB, Xiao XH, Hatzell KB. Effect of pore connectivity on Li dendrite propagation within LLZO electrolytes observed with synchrotron X-ray tomography. ACS Energy Lett. 2018;3(4):1056–61.
10. Randau S, Weber DA, Kotz O, Koerver R, Braun P, Weber A, et al. Benchmarking the performance of all-solid-state lithium batteries. Nat Energy. 2020;5(3):259–70.
11. Chen F, Cao S, Xiang X, Yang D, Zha W, Li J, et al. The Tape-Casting And Pas Sintering Of LLZO Ceramic Membrane Electrolyte. In: Proceeding of the 42nd International Conference on Advanced Ceramics and Composites. 2019; 39(2), pp. 221–30.
12. Gao Z, Mogni LV, Miller EC, Railsback JG, Barnett SA. A perspective on low-temperature solid oxide fuel cells. Energ Environ Sci. 2016;9(5):1602–44.
13. Shen F, Wang R, Tucker MC. Long term durability test and post mortem for metal-supported solid oxide electrolysis cells. J Power Sources. 2020;474:228618.
14. Abdelrasoul A, Doan H, Lohi A, Cheng CH. Morphology control of polysulfone membranes in filtration processes: a critical review. Chembioeng Rev. 2015;2(1):22–43.
15. Kheirieh S, Asghari M, Afsari M. Application and modification of polysulfone membranes. Rev Chem Eng. 2018;34(5):657–93.
16. Yang CP, Zhang L, Liu BY, Xu SM, Hamann T, McOwen D, et al. Continuous plating/stripping behavior of solid-state lithium metal anode in a 3D ion-conductive framework. P Natl Acad Sci USA. 2018;115(15):3770–5.
17. Ren YY, Liu T, Shen Y, Lin YH, Nan CW. Garnet-type oxide electrolyte with novel porous-dense bilayer configuration for rechargeable all-solid-state lithium batteries. Ionics. 2017;23(9):2521–7.
18. Kuang YD, Chen CJ, Kirsch D, Hu LB. Thick electrode batteries: principles, opportunities, and challenges. Adv Energy Mater. 2019;9(33).
19. Fu K, Gong YH, Hitz GT, McOwen DW, Li YJ, Xu SM, et al. Three-dimensional bilayer garnet solid electrolyte based high energy density lithium metal-sulfur batteries. Energ Environ Sci. 2017;10(7):1568–75.
20. Hitz GT, McOwen DW, Zhang L, Ma ZH, Fu ZZ, Wen Y, et al. High-rate lithium cycling in a scalable trilayer Li-garnet-electrolyte architecture. Mater Today. 2019;22:50–7.

21. Shen H, Yi EY, Amores M, Cheng L, Tamura N, Parkinson DY, et al. Oriented porous LLZO 3D structures obtained by freeze casting for battery applications. J Mater Chem A. 2019;7(36):20861–70.

22. Shen H, Yi EY, Heywood S, Parkinson DY, Chen GY, Tamura N, et al. Scalable freeze-tape-casting fabrication and pore structure analysis of 3D LLZO solid-state electrolytes. ACS Appl Mater Inter. 2020;12(3):3494–501.

23. Yi E, Shen H, Heywood S, Alvarado J, Parkinson DY, Chen GY, et al. All-solid-state batteries using rationally designed garnet electrolyte frameworks. ACS Appl Energ Mater. 2020;3(1):170–5.

24. Buannic L, Naviroj M, Miller SM, Zagorski J, Faber KT, Llordes A. Dense freeze-cast $Li_7La_3Zr_2O_{12}$ solid electrolytes with oriented open porosity and contiguous ceramic scaffold. J Am Ceram Soc. 2019;102(3):1021–9.

25. Gordon ZD, Yang T, Morgado GBG, Chan CK. Preparation of Nano- and microstructured garnet Li7La3Zr2O12 solid electrolytes for Li-ion batteries via cellulose templating. ACS Sustain Chem Eng. 2016;4(12):6391–8.

26. Li Z, Sha WX, Guo X. Three-dimensional garnet framework-reinforced solid composite electrolytes with high lithium-ion conductivity and excellent stability. ACS Appl Mater Inter. 2019;11(30):26920–7.

27. Yan JH, Zhao Y, Wang X, Xia SH, Zhang YY, Han YH, et al. Polymer template synthesis of soft, light, and robust oxide ceramic films. iScience. 2019;15:185.

28. Li Y, Zhang W, Dou QQ, Wong KW, Ng KM. $Li_7La_3Zr_2O_{12}$ ceramic nanofiber-incorporated composite polymer electrolytes for lithium metal batteries (vol 7, pg 4190, 2019). J Mater Chem A. 2019;7(8):4190–90.

29. Yang T, Gordon ZD, Li Y, Chan CK. Nanostructured garnet-type solid electrolytes for lithium batteries: electrospinning synthesis of $Li_7La_3Zr_2O_{12}$ nanowires and particle size-dependent phase transformation. J Phys Chem C. 2015;119(27):14947–53.

30. Cheng M, Jiang YZ, Yao WT, Yuan YF, Deivanayagam R, Foroozan T, et al. Elevated-temperature 3D printing of hybrid solid-state electrolyte for Li-ion batteries. Adv Mater. 2018;30(39):1800615.

31. McOwen DW, Xu SM, Gong YH, Wen Y, Godbey GL, Gritton JE, et al. 3D-printing electrolytes for solid-state batteries. Adv Mater. 2018;30(18):1707132.

32. Liu T, Wang Y, Zhang YX, Fang SM, Lei LB, Ren C, et al. Steam electrolysis in a solid oxide electrolysis cell fabricated by the phase-inversion tape casting method. Electrochem Commun. 2015;61:106–9.

33. Lin J, Miao GS, Xia CR, Chen CS, Wang SR, Zhan ZL. Optimization of anode structure for intermediate temperature solid oxide fuel cell via phase-inversion cotape casting. J Am Ceram Soc. 2017;100(8):3794–800.

34. Guillen GR, Pan YJ, Li MH, Hoek EMV. Preparation and characterization of membranes formed by nonsolvent induced phase separation: a review. Ind Eng Chem Res. 2011;50(7):3798–817.

35. Jiang ZY, Xie HQ, Wang SQ, Song X, Yao X, Wang HH. Perovskite membranes with vertically aligned microchannels for all-solid-state lithium batteries. Adv Energy Mater. 2018;8(27):1801433.

36. Yoon KJ, Ye GS, Gopalan S, Pal UB. Cost-effective single step cofiring process for manufacturing solid oxide fuel cells using HSC (TM) anode. J Fuel Cell Sci Tech. 2010;7(2).

37. Dassios KG, Bonnefont G, Fantozzi G, Matikas TE. Novel highly scalable carbon nanotube-strengthened ceramics by high shear compaction and spark plasma sintering. J Eur Ceram Soc. 2015;35(9):2599–606.

38. Jonson RA, Yi E, Shen F, Tucker MC. Optimization of tape casting for fabrication of $Li_{6.25}Al_{0.25}La_3Zr_2O_{12}$ sheets. Energy Fuels. 2021;35(10):8982–90.

39. Huang X, Lu Y, Tin J, Gu S, Xiu TP, Song Z, et al. Method using water-based solvent to prepare $Li_7La_3Zr_2O_{12}$ solid electrolytes. ACS Appl Mater Inter. 2018;10(20):17147–55.

40. Larraz G, Orera A, Sanjuan ML. Cubic phases of garnet-type $Li_7La_3Zr_2O_{12}$: the role of hydration. J Mater Chem A. 2013;1(37):11419–28.

41. El-Shinawi H, Paterson GW, MacLaren DA, Cussen EJ, Corr SA. Low-temperature densification of Al-Doped $Li_7La_3Zr_2O_{12}$: a reliable and controllable synthesis of fast-ion conducting garnets. J Mater Chem A. 2017;5(1):319–29.

42. Zhu YL, Wu S, Pan YL, Zhang XK, Yan ZK, Xiang Y. Reduced energy barrier for Li^+ transport across grain boundaries with amorphous domains in LLZO thin films. Nanoscale Res Lett. 2020;15(1).

43. Xia WH, Xu BY, Duan HN, Guo YP, Kang HM, Li H, et al. Ionic conductivity and air stability of Al-Doped $Li_7La_3Zr_2O_{12}$ sintered in alumina and Pt crucibles. ACS Appl Mater Inter. 2016;8(8):5335–42.

SUPPORTING INFORMATION

Additional supporting information may be found online in the Supporting Information section.